Article

Cell

Cytotoxic T Cells Use Mechanical Force to Potentiate Target Cell Killing

Graphical Abstract

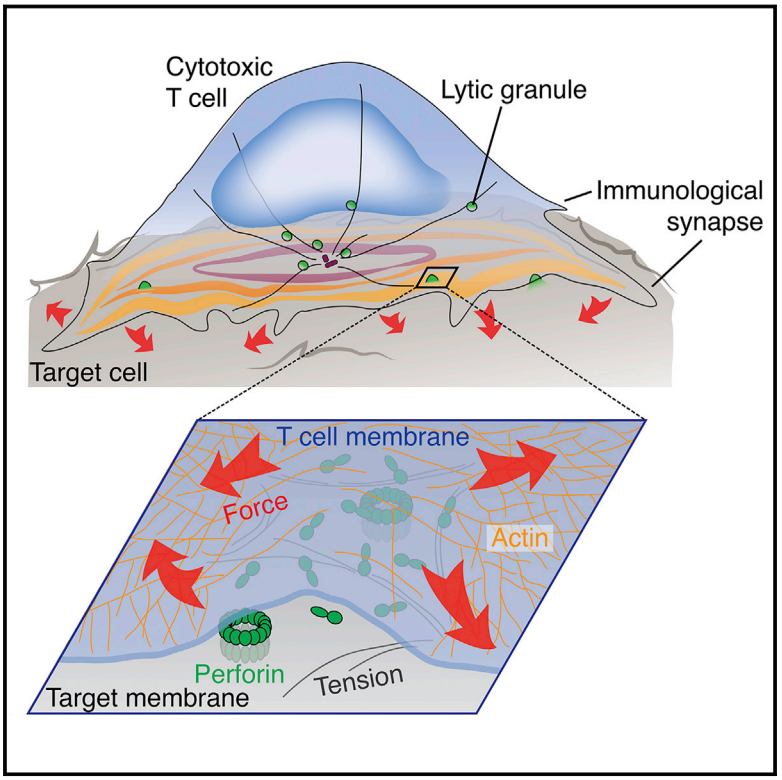

Authors

Roshni Basu, Benjamin M. Whitlock, Julien Husson, ..., Judy Lieberman, Lance C. Kam, Morgan Huse

Correspondence

husem@mskcc.org

In Brief

Cytotoxic T cells exert mechanical force against target cells through the immunological synapse. This potentiates target cell destruction by enhancing the pore-forming activity of the cytolytic molecule perforin.

Highlights

- T cell cytotoxicity correlates with the exertion of mechanical force
- Force exertion is associated with enhanced perforin pore formation on the target cell
- Cell tension promotes perforin pore formation
- Cytotoxic T cells spatiotemporally coordinate force exertion and perforin release

Basu et al., 2016, Cell *165*, 100–110
March 24, 2016
http://dx.doi.org/10.1016/j.cell.2016.01.021

CellPress

Cell

Article

Cytotoxic T Cells Use Mechanical Force to Potentiate Target Cell Killing

Roshni Basu,[1,10] Benjamin M. Whitlock,[2,10] Julien Husson,[3,10] Audrey Le Floc'h,[1] Weiyang Jin,[4] Alon Oyler-Yaniv,[5] Farokh Dotiwala,[6] Gregory Giannone,[7] Claire Hivroz,[8] Nicolas Biais,[9] Judy Lieberman,[6] Lance C. Kam,[4] and Morgan Huse[1,*]

[1]Immunology Program, Memorial Sloan-Kettering Cancer Center, New York, NY 10065, USA
[2]Biochemistry and Molecular Biology Graduate Program, Weill-Cornell Medical College, New York, NY 10065, USA
[3]Hydrodynamics Laboratory (LadHyX), Department of Mechanics, Ecole Polytechnique, Palaiseau 91128, France
[4]Department of Biomedical Engineering, Columbia University, New York, NY 10027, USA
[5]Computational Biology Program, Memorial Sloan-Kettering Cancer Center, New York, NY 10065, USA
[6]Program in Cellular and Molecular Medicine, Harvard Medical School, Boston, MA 02115, USA
[7]CNRS, University of Bordeaux, Interdisciplinary Institute for Neuroscience, UMR 5297, Bordeaux 33000, France
[8]Institute Curie, INSERM U932, PSL Research University, Paris 75005, France
[9]Department of Biology, Brooklyn College of the City University of New York, New York, NY 11201, USA
[10]Co-first author
*Correspondence: husem@mskcc.org
http://dx.doi.org/10.1016/j.cell.2016.01.021

SUMMARY

The immunological synapse formed between a cytotoxic T lymphocyte (CTL) and an infected or transformed target cell is a physically active structure capable of exerting mechanical force. Here, we investigated whether synaptic forces promote the destruction of target cells. CTLs kill by secreting toxic proteases and the pore forming protein perforin into the synapse. Biophysical experiments revealed a striking correlation between the magnitude of force exertion across the synapse and the speed of perforin pore formation on the target cell, implying that force potentiates cytotoxicity by enhancing perforin activity. Consistent with this interpretation, we found that increasing target cell tension augmented pore formation by perforin and killing by CTLs. Our data also indicate that CTLs coordinate perforin release and force exertion in space and time. These results reveal an unappreciated physical dimension to lymphocyte function and demonstrate that cells use mechanical forces to control the activity of outgoing chemical signals.

INTRODUCTION

Cells exchange information through adhesive and highly dynamic cell-cell interactions. Within these contacts, communicative chemical processes are exposed to micrometer scale membrane and cytoskeletal movements capable of imparting substantial mechanical force. It is known that cells use applied force to sense the physical properties of their environment and translate this information into afferent chemical signals that flow into the cell. This process, called mechanotransduction, plays critical roles in the activation and differentiation of multiple cell types (Ingber, 2006; Orr et al., 2006). In principle, force could also modulate intercellular communication, particularly in close cell-cell interactions where movement on one side of the interface induces physical changes on the other side. Whether cell-derived forces actually contribute to the transmission of efferent signals in this manner, however, remains unclear.

Cell-cell contacts in the immune system represent an interesting experimental context for exploring this question because they are structurally dynamic and also mediate a substantial amount of information transfer. One of the most important of these interactions is the immunological synapse (IS) used by cytotoxic T lymphocytes (CTL) to instruct infected or transformed target cells to die. Target cell killing is crucial for adaptive immune responses against intracellular pathogens, and it also plays a central role in several cell-based anti-cancer immunotherapies (Grupp and June, 2011). IS assembly is triggered by the recognition of cognate peptide-major histocompatibility complex (pMHC) on a potential target by T cell receptors (TCRs) on the CTL. Once the IS forms, CTLs secrete a toxic mixture of proteins into the synaptic space that includes perforin and several granzyme proteases (Stinchcombe and Griffiths, 2007). Perforin is a hydrophobic molecule that forms calcium (Ca^{2+})-dependent pores in the target cell membrane. This induces a repair response that enables granzymes to access the target cell cytoplasm, where they induce apoptosis (Keefe et al., 2005; Thiery et al., 2011).

Perforin and granzymes are stored in secretory lysosomes called lytic granules, which cluster around the centrosome in activated CTLs. During IS formation, the centrosome reorients to the center of the contact, placing the granules in close apposition to the synaptic membrane (Stinchcombe et al., 2006). This polarization event is thought to enhance the potency and the specificity of killing by promoting directional release of granule contents toward the target. Recent results, however, indicate that CTLs kill quite effectively in the absence of centrosome reorientation (Bertrand et al., 2013), suggesting there are additional mechanisms by which the IS potentiates cytotoxicity.

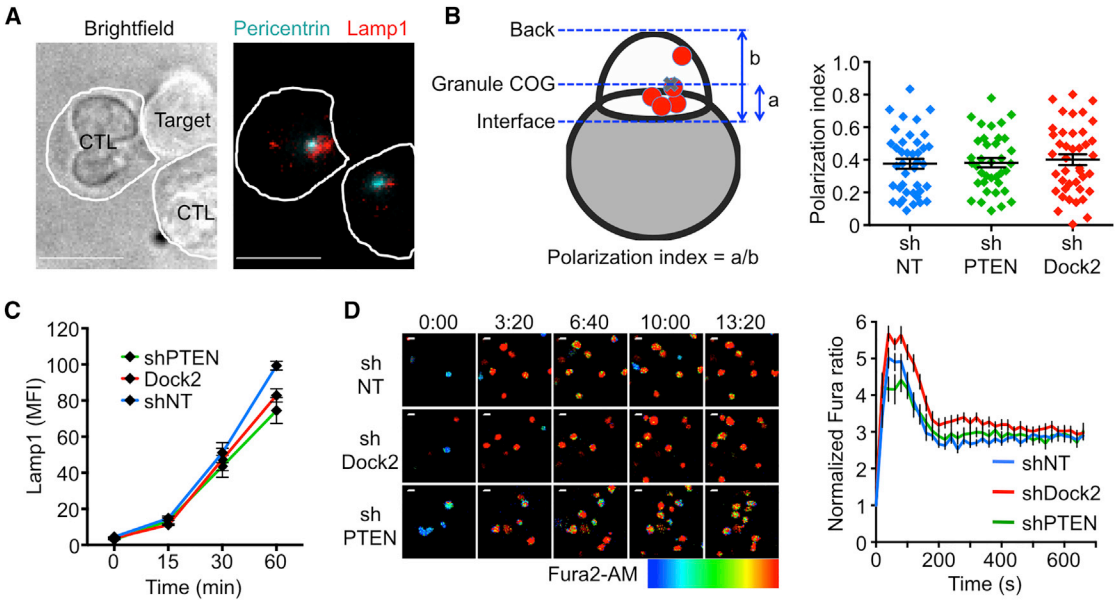

Figure 1. PTEN and Dock2 Are Not Required for Lytic Granule Polarization and Ca^{2+} Flux

(A and B) OT1 CTLs expressing the indicated shRNAs were mixed with OVA-loaded EL4 cells, fixed, and stained for pericentrin and Lamp1 to visualize the centrosome and lytic granules, respectively. (A) Left: brightfield image of a representative CTL-target cell conjugate. Right: corresponding fluorescence image, with white lines indicating CTL boundaries. (B) Left: polarization index was calculated using the center of gravity (COG) of the lytic granules (see Supplemental Experimental Procedures). Right: quantification of lytic granule polarization index ($n \geq 37$ per sample). Differences were not significant (two-tailed Student's t test).

(C) OT1 CTLs expressing the indicated shRNAs were mixed with OVA-loaded EL4 cells and degranulation assessed by surface exposure of Lamp1.

(D) CTLs expressing the indicated shRNAs were loaded with Fura2-AM and imaged on glass surfaces coated with H2-K^b-OVA and ICAM1. Left: representative time-lapse montages of CTLs contacting the stimulatory surfaces. Images are pseudocolored with warmer colors (e.g., orange, red) indicating higher concentrations of intracellular Ca^{2+}. Time in MM:SS is indicated above the montages. Right: mean normalized Fura ratio (see Supplemental Experimental Procedures) graphed against time. $n \geq 21$ cells per sample. All scale bars, 10 μm. Error bars denote SEM. Data are representative of at least two independent experiments.

See also Figure S1.

IS formation also involves intense remodeling of filamentous actin (F-actin), which controls both the growth and the organization of the interface (Le Floc'h and Huse, 2015). Recently, we demonstrated that phosphoinositide 3-kinase (PI3K) activity stimulates actin polymerization within the IS by recruiting Dock2, an exchange factor for the Rho GTPase Rac (Le Floc'h et al., 2013). CTLs lacking Dock2 form miniaturized synapses that are structurally unstable. Conversely, depletion of PTEN, a lipid phosphatase that antagonizes PI3K, markedly enhances IS growth. Interestingly, whereas Dock2-deficient CTLs kill target cells poorly, PTEN-deficient CTLs exhibit dramatically enhanced cytotoxicity (Le Floc'h et al., 2013). These results establish an intriguing link between target cell killing and F-actin remodeling at the IS. The mechanistic basis for this relationship, however, has remained unclear.

Synaptic F-actin is highly dynamic, exhibiting constant retrograde flow toward the center of the IS as well as bursts of anterograde flow in the opposite direction (Bunnell et al., 2001; Grakoui et al., 1999; Ritter et al., 2015). These and other effects enable the T cell to impart nanonewton scale forces against the target cell (Bashour et al., 2014; Husson et al., 2011). In the present study, we combined specific perturbations of PI3K-Dock2 signaling with single cell biophysical approaches to investigate the impact of synaptic forces on CTL function. We found that force exertion at the IS potentiates killing by straining the target cell surface and thereby enhancing the pore forming activity of perforin. These results demonstrate that T cells mix physical and chemical outputs to enhance their effector responses and reveal an unexpected role for cellular mechanics in intercellular communication.

RESULTS

Cytotoxicity Correlates with Synaptic Force Exertion

The killing phenotypes observed in PTEN- and Dock2-deficient CTLs implied an important role for PI3K-dependent F-actin remodeling in cellular cytotoxicity. To investigate this relationship, we first examined the distribution of lytic granules in CTL-target cell conjugates. CTLs expressing the OT1 TCR, which recognizes the ovalbumin$_{257–264}$ peptide (OVA) bound to the class I MHC molecule H2-K^b, were transduced with short hairpin RNA (shRNA) against PTEN (shPTEN) or Dock2 (shDock2) or with nontargeting control shRNA (shNT) (Figure S1). They were then mixed with OVA-loaded EL4 target cells and the resulting conjugates fixed and stained to visualize lytic granules (Figure 1A). Suppression of Dock2 or PTEN had no effect on granule polarization to the IS (Figure 1B), indicating that intracellular trafficking of cytotoxic cargo does not involve PI3K-Dock2 signaling. We

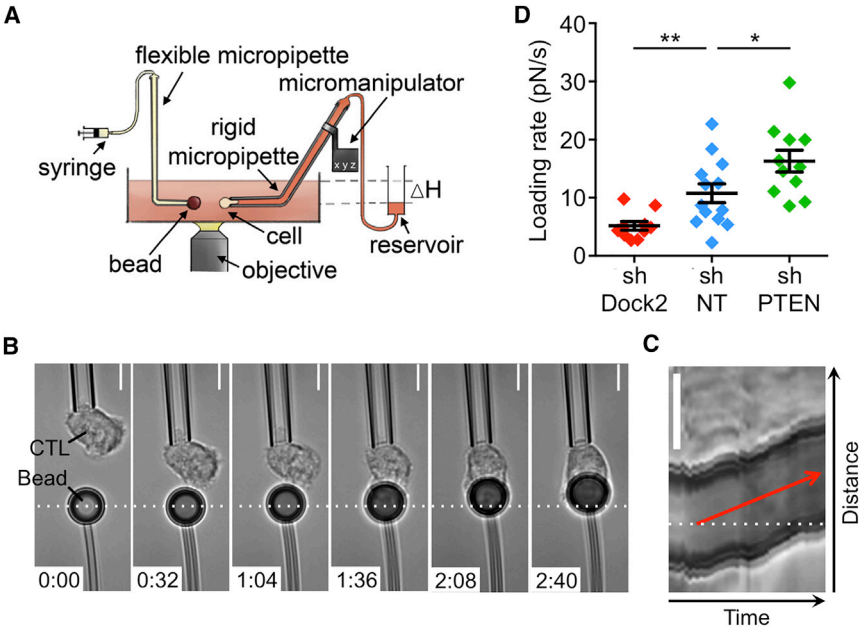

Figure 2. PI3K Signaling Controls Force Exertion Perpendicular to the IS

(A) Schematic diagram of the micropipette-based system.

(B) Time-lapse montage of a representative micropipette experiment. Dashed white line denotes the initial position of the bead. Time is indicated in M:SS in the bottom left corner of each image.

(C) Kymograph of the experiment shown in (B). The loading rate can be derived from the slope of the red line.

(D) Average loading rate during the pulling phase of the response, calculated for cells expressing the indicated shRNAs. Error bars denote SEM. n ≥ 10 cells per condition. *p < 0.05, **p < 0.01, calculated by two-tailed Mann-Whitney test. All scale bars, 5 μm. Data are representative of at least two independent experiments.

See also Movie S1.

also quantified granule release (called degranulation) from CTLs by measuring surface exposure of the granule resident protein Lamp1 after stimulation with target cells. This response was unaffected by depletion of PTEN or Dock2 (Figure 1C), consistent with previous results (Le Floc'h et al., 2013). Finally, we examined TCR-induced calcium (Ca^{2+}) flux, a requisite step for granule clustering and exocytosis (Beal et al., 2009; Ostergaard et al., 1987), by imaging CTLs on glass surfaces coated with H2-K^b-OVA and ICAM1 (a ligand for the $\alpha_L\beta_2$ integrin LFA1). Dock2- and PTEN-deficient CTLs displayed robust Ca^{2+} responses that were comparable to those of shNT expressing controls (Figures 1D and 1E). Taken together, these data indicate that suppression of PTEN and Dock2 does not affect granule polarization and fusion at the IS, implying that these perturbations influence cytotoxicity via a different mechanism.

Force exertion across the IS could, in principle, provide a physical avenue for control of target cell killing. To investigate this possibility, we first asked whether PI3K-Dock2 signaling, which controls cytotoxic efficiency, might also regulate IS mechanics. Accordingly, we compared synaptic force exertion in OT1 CTLs transduced with shNT, shPTEN, and shDock2. To measure forces perpendicular to the IS, we used micropipettes to place individual CTLs in contact with polystyrene beads coated with H2-K^b-OVA and ICAM1 (Figure 2A). Subsequent bead displacements toward or away from the CTL were translated into force measurements using the known stiffness of the micropipette holding the bead (see Experimental Procedures). Contact with stimulatory beads induced a rapid CTL spreading response not unlike IS formation with a target cell. Spreading was frequently accompanied by transient pushing of the bead away from its initial position. This was followed in almost all cases by a pronounced pulling phase in which the bead became engulfed by the CTL (Figure 2B; Movie S1). Analysis of kymographs derived from each experimental trial enabled us to determine the rate of bead movement during the pulling phase of the response (Figure 2C), which is proportional to the pulling force. This parameter, called the loading rate, was significantly enhanced in CTLs lacking PTEN and markedly reduced in CTLs lacking Dock2 (Figure 2D). These results indicate that PI3K-Dock2 signaling drives force exertion perpendicular to the CTL-target cell interface.

To measure forces in the plane of the IS, we imaged OT1 CTLs on arrays of polydimethylsiloxane (PDMS) micropillars bearing immobilized H2-K^b-OVA and ICAM1 (Figure 3A) (Bashour et al., 2014). Because the dimensions (6 μm tall, 0.7 μm diameter) and composition of these pillars were known, observed pillar deflections could be converted into force vectors. OT1 CTLs exhibited cell spreading and OVA-induced Ca^{2+} flux upon contact with the arrays, consistent with canonical TCR activation and signaling (Figures 3B and S2A). In most cells, spreading was associated with centrifugal pillar deflections, indicative of outwardly oriented forces (Figures 3B and 3C; Movie S2). After the size of the interface stabilized, these deflections tended to reverse polarity and point inward. The progression from centrifugal "spreading" to centripetal "squeezing" was reminiscent of the responses displayed by naive $CD4^+$ T cells on pillar arrays (Bashour et al., 2014). However, OT1 CTLs exerted substantially more force per pillar than naive cells (Figure 3D) (Bashour et al., 2014), and their force profiles were less symmetric. Indeed, instantaneous force exertion tended to be concentrated in "hotspots" characterized by the strong deflection of one to three pillars (Figure 3B, green asterisks). Importantly, suppression of PTEN markedly enhanced force exertion on both individual pillars and also the entire array (Figures 3E and S2B). Dock2 suppression gave less conclusive results, with some experiments revealing a slight inhibitory effect and others indicating no significant difference (Figures 3F and S2B). It is possible that forces in the plane of the IS are less sensitive to reduced PI3K signaling than those in the orthogonal dimension. Nevertheless, when taken together with our micropipette data, these

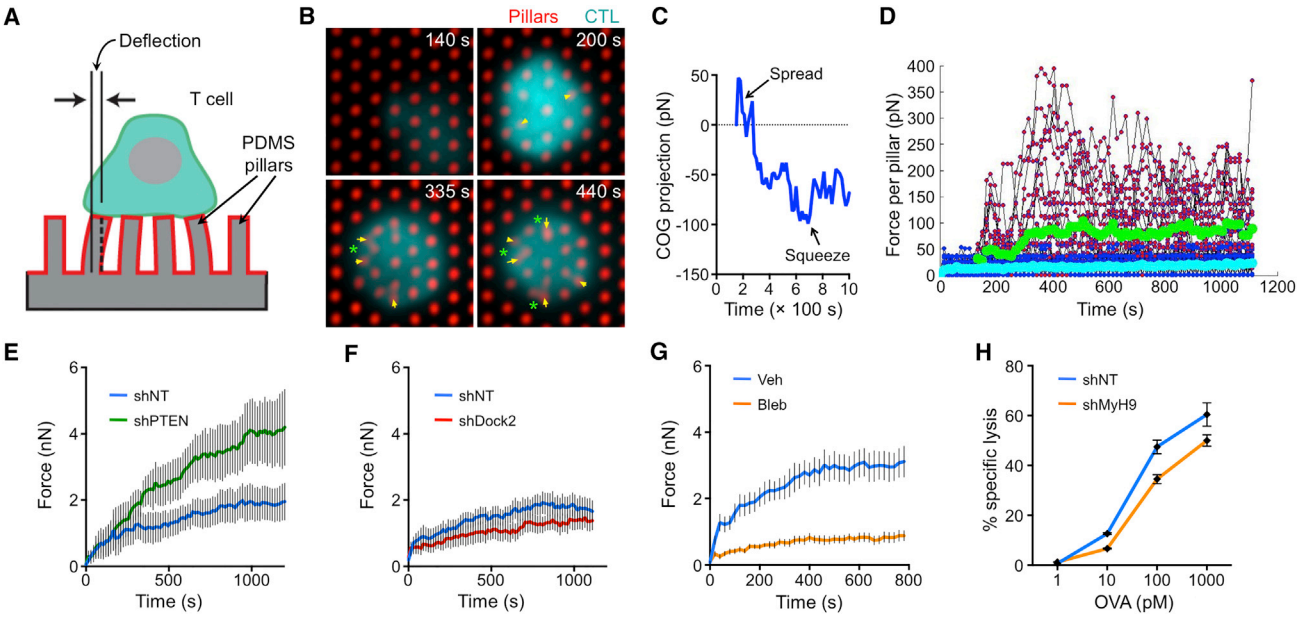

Figure 3. PI3K Signaling and NMII Control Force Exertion Parallel to the IS

(A) Schematic diagram of the micropillar system.

(B–F) CTLs expressing shNT, shDock2, or shPTEN were imaged on stimulatory micropillar arrays. (B) Time-lapse montage of a representative CTL-micropillar interaction. Time is indicated in the top right corner of each image. Large pillar deflections are indicated by yellow arrows. Green asterisks denote "hotspots" of strong force exertion. (C) Average projection of pillar deflections along the line connecting each pillar to the cell's center of gravity (COG projection) was determined for the CTL shown in (B) and plotted against time. (D) Aggregate plot of instantaneous force per pillar exerted by the CTL in (B), graphed against time. Pink dots denote pillars in contact with the cell, and blue dots denote pillars outside of the interface. Average force per pillar within the interface is shown in green and background force per pillar in cyan. (E and F) Total force exertion against the pillar array graphed versus time for CTLs expressing the indicated shRNAs. $n \geq 6$ cells per sample.

(G) CTLs treated with 50 μM blebbistatin (Bleb) or vehicle control (Veh) were imaged on stimulatory micropillar arrays. Total force exertion against the array is graphed as in (E).

(H) CTLs expressing the indicated shRNAs were mixed 1:1 with OVA-loaded RMA-s cells. Specific lysis is graphed as a function of OVA concentration. All error bars denote SEM. Data are representative of at least two independent experiments.

See also Figure S2 and Movie S2.

studies indicate that CTLs exert multidimensional PI3K-dependent forces against the target cell.

Myosin-based contractility is crucial for the generation of actin-dependent forces in multiple cell types, and clusters of the nonmuscle myosin II (NMII) isoform have been observed within the T cell IS (Babich et al., 2012; Jacobelli et al., 2004; Yi et al., 2012). Although the precise function of synaptic NMII remains controversial (Hammer and Burkhardt, 2013), it is appropriately positioned to contribute to force exertion. To investigate this possibility, we examined micropillar deflection in the presence of blebbistatin, a small molecule myosin II inhibitor. Blebbistatin treatment dramatically reduced force exertion during both the "spreading" and "squeezing" phases of the response (Figures 3G and S2C), indicative of an important role for NMII in IS mechanics. Next, we asked whether synaptic force exertion by NMII modulates cytotoxicity. For these experiments, we utilized shRNA knockdown of the myosin heavy chain MyH9 (shMyH9) to target the NMII complex selectively in CTLs. This strategy yielded only partial suppression of MyH9 (Figure S2D), as previously reported (Liu et al., 2013). CTLs expressing shMyH9 exhibited a subtle, but consistent killing defect that paralleled the partial knockdown of the protein (Figure 3H). Importantly, TCR-induced degranulation was not inhibited in these cells (Figure S2E), indicating that TCR activation and signaling remained intact. We conclude that myosin activity, like PI3K signaling, controls both cytotoxicity and synaptic force exertion.

PI3K Signaling Accelerates Perforin Pore Formation

Next, we re-examined how PI3K signaling affects cytotoxicity, focusing on events that occur downstream of perforin and granzyme secretion. Perforin initiates killing by forming plasma membrane pores on the target cell (Pipkin and Lieberman, 2007). This event can be visualized by imaging CTLs and target cells in the presence of high concentration (100 μM) propidium iodide (PI) (Keefe et al., 2005; Lopez et al., 2013). Plasma membrane perforation allows PI to access the cytoplasm, rendering the target cell fluorescent (Figure 4A). To quantify the rate of perforin pore formation using this approach, we imaged OVA-loaded RMA-s target cells together with OT1 CTLs in 50 × 50 μm PDMS microwells, which facilitate extended observation of individual CTL-target cell interactions (Figure 4B; Movie S3). These experiments revealed that CTLs expressing shPTEN were significantly more effective at inducing perforin pore formation than

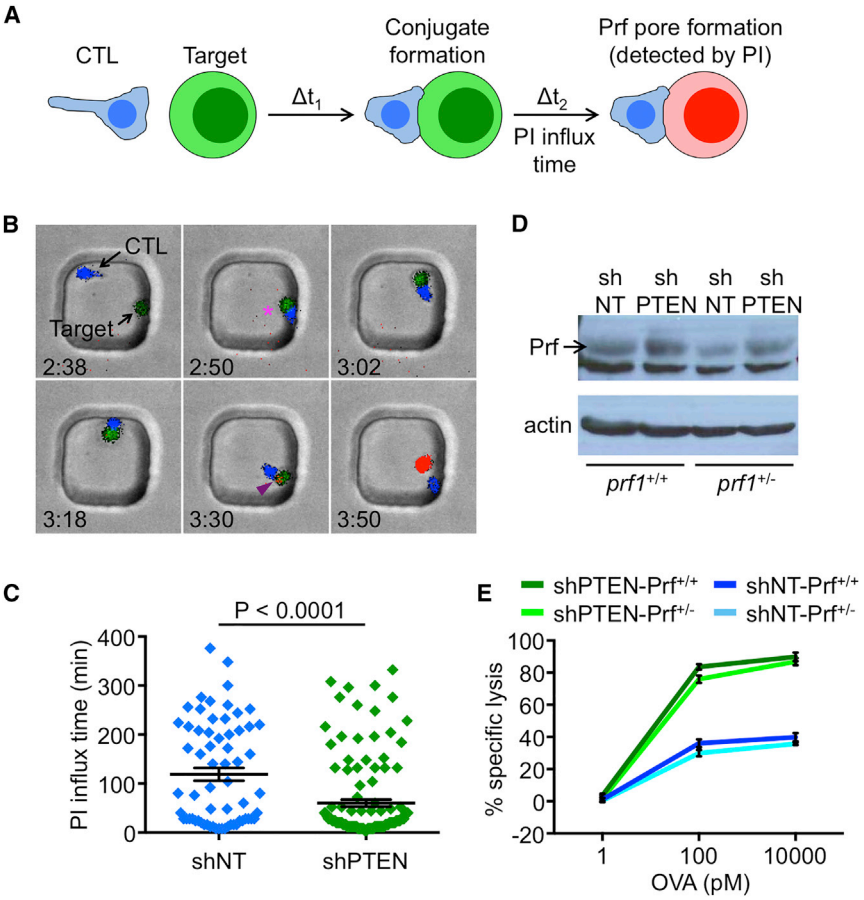

Figure 4. PTEN Deficiency Enhances Perforin Pore Formation

(A) Schematic diagram showing perforin pore detection by PI.

(B and C) CTLs expressing shNT or shPTEN together with cyan fluorescent protein (CFP) were mixed with carboxyfluorescein succinimidyl ester (CFSE)-labeled, OVA-loaded RMA-s cells and imaged in PDMS microwells in the presence of 100 μM PI. (B) Time-lapse montage of a representative microwell showing conjugate formation (magenta asterisk) and PI influx (purple arrowhead). Time is indicated in H:MM in the bottom left corner of each image. (C) Time between conjugate formation and PI influx (PI influx time) quantified for shNT and shPTEN expressing CTLs. Error bars denote SEM. n ≥ 65 conjugates per sample. P value calculated by two-tailed Mann-Whitney test.

(D) Perforin (Prf) expression in the indicated CTLs was analyzed by western blot. Actin served as a loading control.

(E) *prf1*$^{+/+}$ and *prf1*$^{+/-}$ CTLs expressing the indicated shRNAs were mixed 1:1 with OVA-loaded RMA-s cells. Specific lysis is graphed as a function of OVA concentration. Data are representative of at least two independent experiments.

See also Movie S3.

shNT expressing controls. The fraction of interactions associated with target cell PI incorporation was higher (93% for shPTEN CTLs versus 71% for shNT CTLs), and among these, the time delay between IS formation and PI fluorescence (influx time) was significantly reduced (Figure 4C).

CTLs lacking PTEN exhibited higher total levels of perforin protein (Figure 4D), which could, in principle, explain the enhanced pore formation we observed. This increase in perforin expression could be reversed, however, by removing one copy of the *prf1* gene in the context of PTEN deficiency. Importantly, killing by PTEN-deficient *prf1*$^{+/-}$ CTLs was essentially equivalent to that of PTEN-deficient *prf1*$^{+/+}$ CTLs and substantially greater than that of *prf1*$^{+/+}$ shNT controls (Figure 4E). Hence, it is unlikely that the accelerated pore formation seen in the absence of PTEN resulted from changes in perforin expression. Rather, PTEN suppression appeared to boost cytotoxicity by increasing perforin activity on a per molecule basis.

Cell Tension Potentiates Target Cell Lysis

Biophysical studies have shown that increasing the tension of target membranes boosts the activity of pore forming peptides, implying that tangential force can reduce the energetic cost of inserting a hydrophobic molecule into the bilayer (Huang et al., 2004; Lee et al., 2008; Polozov et al., 2001). Accordingly, we reasoned that synaptic forces might potentiate perforin pore formation by applying tension to the target cell. To explore the relationship between cell tension and perforin function, we grew adherent cells on polyacrylamide hydrogels of varying elasticity (Engler et al., 2006). Cell tension in this culture system mirrors the underlying hydrogel; stiff hydrogels enforce high tension, while soft hydrogels induce the opposite effect (Chan and Odde, 2008; Hui et al., 2015; Lo et al., 2000; Oakes et al., 2009). Consistent with this principle, we found that B16 melanoma cells adopted a stellate architecture on stiff (E = 50 kPa) hydrogels characteristic of high tension, while on soft (E = 12 kPa) hydrogels they displayed a more collapsed morphology (Figure S3). To assess perforin pore formation under each condition, we treated the cells with purified perforin protein (~1 μg/ml) in the presence of 100 μM PI (Figure 5A). Although the capacity of perforin to induce PI influx varied from day to day (see Supplemental Experimental Procedures), we consistently observed that cells on 50 kPa substrates were more sensitive to pore formation than those on 12 kPa substrates, implying that increased cell tension potentiates perforin activity (Figures 5B, 5C, and S4A; Movies S4 and S5).

Next, we investigated whether target cell tension similarly modulates CTL-mediated killing. OT1 CTLs were added to OVA-loaded B16 cells grown on stiff or soft substrates and target cell lysis measured by the release of lactate dehydrogenase (LDH), a cytoplasmic enzyme (Figure 5D). Killing was significantly enhanced on 50 kPa hydrogels relative to 12 kPa hydrogels, despite equivalent levels of TCR-induced degranulation (Figures

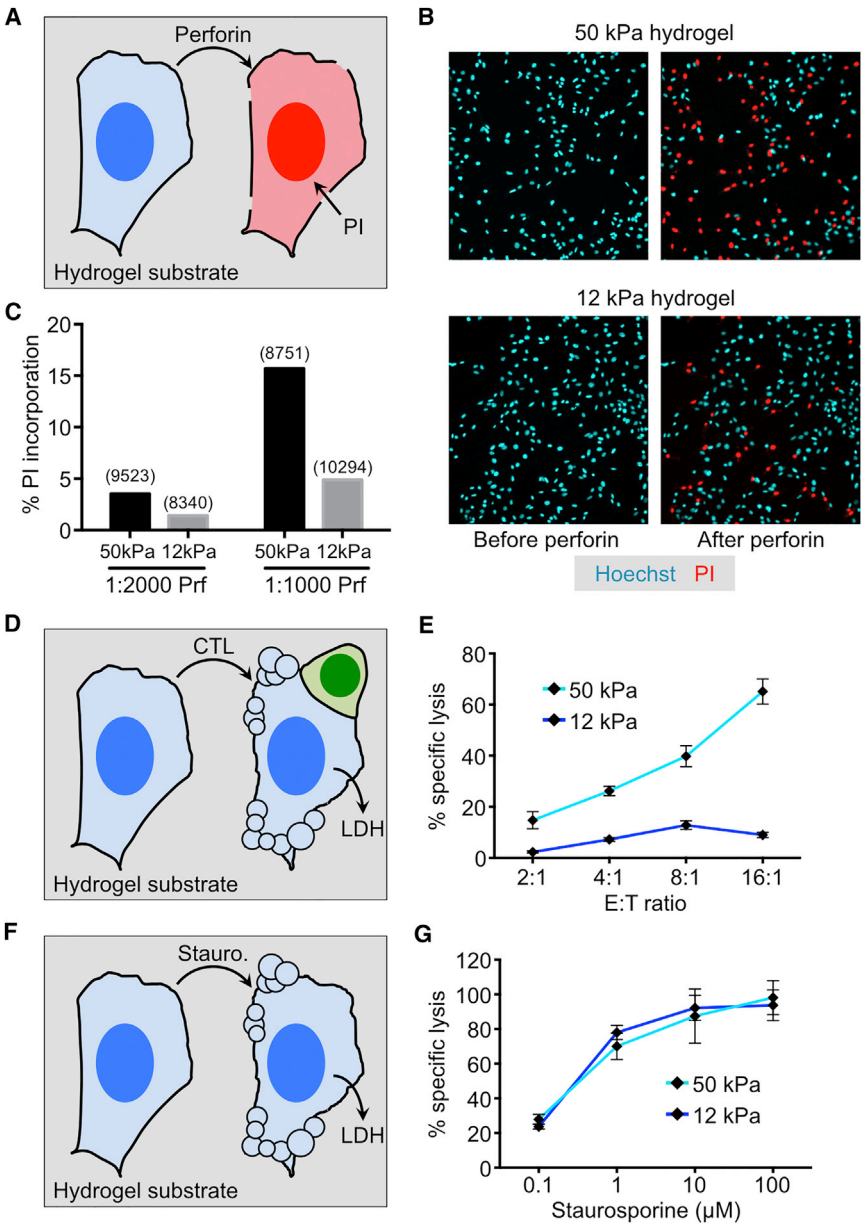

Figure 5. Cell Tension Promotes Perforin Pore Formation and CTL-Mediated Killing

(A–C) B16 cells were cultured overnight on stiff (E = 50 kPa) or soft (E = 12 kPa) hydrogels, stained with Hoechst 33342, and treated with the indicated dilutions of perforin (1:1,000 ≈1 μg/ml final concentration) in the presence of 100 μM PI. (A) Schematic diagram of the perforation assay. (B) Representative images before and after perforin treatment on both stiff (top) and soft (bottom) hydrogels. Perforated cells were identified by their PI^+ nuclei. (C) Quantification of a representative perforation experiment on hydrogels. Total cell counts are shown in parentheses above each bar. (D) Schematic diagram of a B16 killing assay on hydrogel substrate.

(E) OT1 CTLs were added to OVA-loaded B16 cells grown on stiff or soft hydrogels. Specific lysis was quantified by LDH release at the indicated effector to target (E:T) ratios.

(F) Schematic diagram of staurosporine-induced apoptosis on hydrogel substrate.

(G) B16 cells grown on stiff or soft hydrogels were exposed to the indicated concentrations of staurosporine. Apoptosis was quantified by LDH release. Error bars denote SEM. Data are representative of at least two independent experiments. See also Figures S3, S4, and S5 and Movies S4 and S5.

5E and S5). Importantly, target cell killing by the small molecule staurosporine, which induces apoptosis in multiple cell types, was unaffected by substrate elasticity (Figures 5F and 5G). B16 cells grown on stiff matrices are therefore not intrinsically less viable. Rather, they are selectively sensitized to perforin-dependent killing.

Cell tension is imposed both by the cytoskeletal cortex and by the plasma membrane. To determine the relative contributions of membrane and cortical tension to perforin function, we assessed pore formation in the presence of reagents that alter the two parameters differentially (Figure 6A). Blebbistatin, by inhibiting myosin II, reduces cortical tension while increasing membrane tension (Houk et al., 2012; Lee et al., 2011). By contrast, the actin depolymerization agent latrunculin A reduces both parameters (Masters et al., 2013; Wakatsuki et al., 2001). Treatment of adherent B16 cells with latrunculin A substantially decreased pore formation by purified perforin, while blebbistatin reproducibly enhanced it (Figures 6B, S4B, and S4C). These results suggested that membrane tension, rather than cortical tension, controls perforin activity. To further test this idea, we treated cells with hypotonic and hypertonic buffers, which increase and decrease, respectively, membrane tension (Houk et al., 2012) (Figure 6C). Pore formation was enhanced by hypotonic buffer and suppressed by hypertonicity (Figures 6D and S4D), further supporting the idea that perforin and membrane tension function synergistically.

Synaptic Force Exertion Is Coordinated with Degranulation

Finally, we examined whether perforin release is spatiotemporally correlated with the application of force at the IS, using a degranulation probe containing a pH-sensitive GFP (pHluorin) attached to the C-terminal domain of Lamp1 (Rak et al., 2011). pHluorin-Lamp1 is sorted into lytic granules, where its fluorescence is quenched by the acidic environment. Granule fusion with the plasma membrane, however, neutralizes the pH around the pHluorin, allowing it to fluoresce. When CTLs expressing pHluorin-Lamp1 were imaged on PDMS micropillars coated

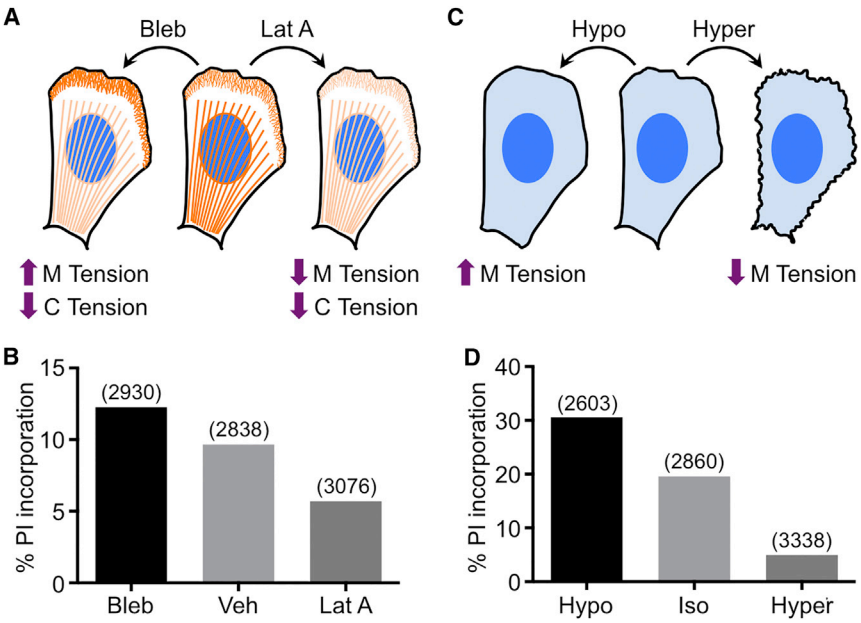

Figure 6. Membrane Tension Potentiates Perforin Pore Formation

(A) Diagram schematizing the effects of blebbistatin (Bleb) and latrunculin A (Lat A) on cortical (C) and membrane (M) tension. Lamellipodial F-actin and stress fibers are indicated in orange.

(B) B16 cells cultured on plastic were treated with perforin (1:1,000 dilution) in the presence of 100 μM PI and either 100 μM Bleb, 7.5 μM Lat A, or vehicle control (Veh) as indicated. Perforation was quantified by PI incorporation.

(C) Diagram schematizing the effects of hypotonic (Hypo) or hypertonic (Hyper) medium on membrane tension.

(D) B16 cells cultured on plastic were treated with perforin (1:1,000 dilution) in the presence of 100 μM PI either in isotonic (Iso), hypotonic, or hypertonic medium as indicated. Perforation was quantified by PI incorporation. In (B) and (D), total cell counts are shown in parentheses above each bar. Data are representative of three independent experiments.

See also Figure S4.

with H2-K^b-OVA and ICAM1, degranulation events appeared as abrupt increases in green fluorescence within the interface between the CTL and the array (Figures 7A and 7B). Most events occurred within 5 min of initial contact (Figure 7C) and many seemed to be closely associated with hotspots of strong force exertion (Figure 7D).

To quantify the relationship between degranulation and force, we computed the distance between each granule fusion event and the closest pillar experiencing strong deflections during that time (called the distance to displaced pillar [DDP]; see Experimental Procedures). We then compared each value to a null distribution generated by performing the DDP calculation for every x-y position within the interface between the CTL and the array (Figure 7E). DDP values associated with degranulation events were significantly lower than the mean values of their paired null distributions, indicating that the observed coupling between granule release and pillar deflection did not occur by chance (Figure 7F). We also quantified the radial distribution of degranulation and force exertion within the IS (Figure 7G) and found that both parameters were enriched within an annular region slightly more than halfway between the center of the IS and its outer edge (Figures 7H and 7I). Taken together, these results suggest that CTLs spatiotemporally coordinate cytolytic secretion with the local application of force, and they also identify a domain within the IS in which these interactions occur.

Could forces within this degranulation zone apply enough membrane tension to potentiate perforin pore formation? To address this question, we first determined the membrane tension change necessary to sensitize a cell to perforin. Using an established approach in which an optical trap is used to pull a thin tether of membrane from the cell surface (Dai and Sheetz, 1995) (Figures S6A and S6B), we calculated the membrane tension of adherent B16 cells to be 100 μN/m. In the presence of latrunculin A, which protects cells from perforin pore formation (Figures 6B and S4B), membrane tension decreased to 15 μN/m. These data suggest that an ~85 μN/m difference in membrane tension (equivalent to 85 × 10^{-18} J/μm^2) is sufficient to make perforin pore formation more energetically favorable (Figure S6C). Assuming a pore size of 15 nm, this tensional difference implies a free energy change of 1.5 × 10^{-20} J per pore (see Experimental Procedures). In micropillar experiments, we routinely observed pillar deflections of >1 μm within force exertion hotspots. Each of these strong deflections required >340 pN of force (Figure 3D), implying the transfer of >170 × 10^{-18} J of mechanical energy (see Experimental Procedures) within an ~1 μm^2 region of the array. This degree of energy transmission (170 × 10^{-18} J/μm^2) compares favorably with the tensional change (85 × 10^{-18} J/μm^2) demonstrated by the tether experiments to modulate perforin activity, and it would be sufficient, in principle, to mechanically potentiate a large number of pores. Hence, under conditions of close synaptic contact, CTLs should be capable of locally sensitizing the target cell membrane to perforin.

DISCUSSION

Communication between immune cells is generally presented as a chemical process based on ligand recognition by receptors. It is becoming increasingly clear, however, that mechanical forces at cell-cell interfaces are necessary both to enable and to regulate communicative chemical interactions. Recent studies have documented the importance of cytoskeletally driven pulling for receptor activation and antigen uptake (Comrie et al., 2015; Liu et al., 2014; Natkanski et al., 2013), which are both processes that mediate information flow into the lymphocyte. Our results demonstrate that physical forces can also modulate information flow out of the cell, in this case by potentiating the activity of a secreted protein, perforin. This synergy between applied force and outgoing chemical signals, which we term mechanopotentiation, conceptually expands the purview of cellular mechanics

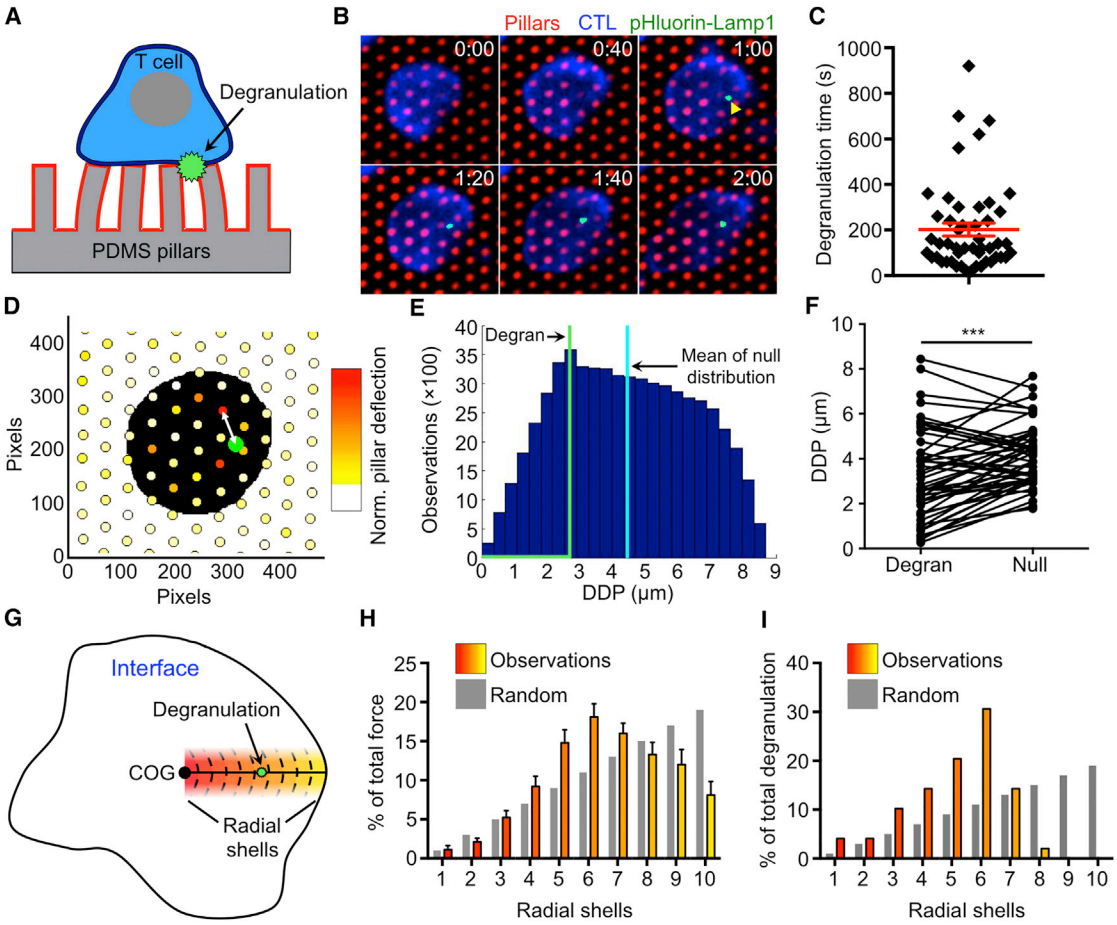

Figure 7. Degranulation Is Spatiotemporally Correlated with Force Exertion at the IS

(A) Diagram schematizing fluorescent detection of degranulation during a micropillar experiment.

(B–I) CTLs expressing pHluorin-Lamp1 were imaged on stimulatory micropillar arrays. (B) Representative time-lapse montage showing pillar deflections during a degranulation event (indicated by the yellow arrowhead). Time is indicated in M:SS in the top right corner of each image. (C) Graph of the offset time between contact formation and degranulation (degranulation time). (D) Graphical representation of the pillar array in (B), with the degranulation position depicted as a green circle and the cell envelope at the moment of degranulation shown in black. Pillars are color-coded based on their average deflection during the degranulation. Warmer colors (e.g., orange, red) denote stronger deflections. The DDP for this degranulation is indicated by the double-headed white arrow. (E) Histogram plot derived from the experiment in (B) showing the DDP for each position in the CTL interface. The mean value for the distribution is denoted by the vertical cyan line. The vertical green line indicates the DDP for the degranulation itself. (F) DDPs of degranulation (Degran) were compared to the mean values of their paired null distributions. ***$p < 0.001$, calculated by two-tailed paired t test. (G) Schematic diagram of the CTL-array interface showing the radial shells used for spatial analysis. (H and I) The radial distribution of total force exertion (H) and degranulation position (I) in degranulating cells. Color-coding of the bars corresponds to the shells shown in (G). Gray bars indicate the spatial distribution that would be expected by chance (outer shells are larger than inner ones). All error bars denote SEM. For (C), (F), and (I), n = 49 degranulation events pooled from three independent experiments.

See also Figure S6.

as an active mediator of not only afferent but also efferent intercellular communication.

It has been proposed that the IS enhances the intensity and specificity of intercellular communication by restricting the diffusion of secreted factors (Huse et al., 2006; Stinchcombe and Griffiths, 2007; Woodsworth et al., 2015). Studies of cytokine-mediated communication, however, indicate that soluble proteins escape the T cell-target cell interface very quickly (Feinerman et al., 2010; Müller et al., 2012; Sanderson et al., 2012). An alternative strategy for boosting selectivity and efficiency would involve locally increasing the specific activity of secreted molecules. Synaptic mechanopotentiation of perforin pore formation falls into this second class of mechanisms. Synergy between force exertion and perforin activity would reduce the amount of degranulation required for each killing event and thereby limit bystander damage resulting from excessive cytolytic secretion. It would also facilitate serial killing by enabling CTLs to reserve perforin and granzyme for other targets. We expect that other cytotoxic lymphocytes will also employ this strategy.

Our results demonstrate that NMII is critical for force exertion at the IS. This is surprising given that myosin activity is dispensable

for IS formation and only modestly affects synaptic architecture (Babich et al., 2012; Jacobelli et al., 2004; Yi et al., 2012). We also found that depletion of NMII reduced CTL-mediated cytotoxicity, implying that myosin-dependent forces contribute to mechanopotentiation during target cell killing. Although we favor this interpretation, it must be noted that CTLs lacking NMII also exhibit delayed centrosome polarization (Liu et al., 2013). A partial polarity defect could affect cytotoxicity by altering the directionality of cytolytic secretion. Hence, at this stage we cannot attribute the killing phenotype of NMII-deficient cells solely to a defect in force exertion.

Perforin pores drive target cell killing by inducing a membrane repair response that stimulates the uptake of additional perforin and granzymes (Keefe et al., 2005; Thiery et al., 2011). Although the methods used in this study assessed the effects of cellular mechanics on initial pore formation, they did not address whether force might also modulate membrane repair downstream. Membrane tension has been implicated in the regulation of both exo- and endocytosis in multiple cell types (Diz-Muñoz et al., 2013). It is therefore quite plausible that CTL-induced distortions within the IS could influence membrane repair and in this manner control not only the initiation but also the progression of cytotoxicity.

F-actin accumulates in the periphery of the IS and is depleted from the center, forming a stereotyped annular pattern (Le Floc'h and Huse, 2015). Lytic granules cluster beneath the center of the F-actin ring, and it has been proposed that they release their contents primarily by fusing with the actin-free plasma membrane in this region (Stinchcombe and Griffiths, 2007; Stinchcombe et al., 2006). Using a fluorescent probe for degranulation, we found that cytolytic secretory events are not enriched in the very center of the IS, but rather in an intermediate domain that overlaps with the region of strongest force exertion. In the canonical IS, this intermediate zone is occupied by the inner aspect of the F-actin ring and clusters of integrins (Dustin et al., 2010); it therefore contains the adhesive and cytoskeletal machinery required to transmit force. Super-resolution imaging studies have demonstrated that this zone can also accommodate the formation of actin hypodense regions of plasma membrane suitable for vesicle fusion (Brown et al., 2011; Rak et al., 2011). Accordingly, we favor a model in which degranulation occurs at the border between the central F-actin-depleted area and the peripheral F-actin ring. This would enable the CTL to balance the physical requirements of exocytosis with the benefits of synaptic mechanopotentiation.

The striking spatiotemporal correlation we observed between lytic granule release and force exertion suggests that CTLs create local mechanical hotspots on the target cell surface that are particularly sensitive to perforin. Although the fluid nature of lipid bilayers generally promotes rapid equilibration of applied force, local interactions with the cytoskeleton have been shown to generate inhomogeneities in tension (Diz-Muñoz et al., 2013). The idea that physical inhomogeneities of this kind could be established within dynamic and strongly adhesive interfaces, such as the IS, is quite intriguing, and represents an interesting topic for future studies.

The mechanical component of cytotoxicity could be particularly important in the context of anti-cancer immunity. Within solid tumors, cells tend to be stiffer because of enhanced cytoskeletal contractility and extracellular matrix rigidity (Paszek et al., 2005). Although increased stiffness would be expected to promote CTL-mediated killing, any advantage gained by the immune system would likely be overwhelmed by the tolerogenic signals that prevail within the tumor microenvironment (Rabinovich et al., 2007). During metastatic dissemination, however, cells from the tumor move away from this immunosuppressive milieu. In that regard, it is interesting to note that isolated cancer cells tend to be softer than their non-transformed counterparts (Guck et al., 2005; Hou et al., 2009; Xu et al., 2012). This deformability could enable them to resist immune-mediated attack when outside of the tumor microenvironment.

The intricate cytoskeletal dynamics of lymphocyte synapses include both actin flows that propagate in the plane of the interface (Bunnell et al., 2001; Grakoui et al., 1999; Ritter et al., 2015) and filopodial protrusions that can deform the surface of the target cell (Sage et al., 2012; Ueda et al., 2011). As we work to define the functional relevance of these and other structures, it will be important to consider their capacity to transmit information physically during the effector phase of lymphocyte responses. Mechanical forces are well suited for rapid and highly compartmentalized signaling within cell-cell interfaces and as such, they represent a valuable mode of intercellular communication in complex environments.

EXPERIMENTAL PROCEDURES

Additional methods may be found in Supplemental Experimental Procedures.

Animal Use

The animal protocols used for this study were approved by the Institutional Animal Care and Use Committee of Memorial Sloan-Kettering Cancer Center.

Micropipette-Based Force Measurements

Stimulatory beads were prepared by coating 6-μm diameter streptavidin-coated polystyrene particles (Spherotech) with biotinylated H2-K^b-OVA and ICAM1 (1 μg/ml each) for 2 hr in 20 mM HEPES pH 7.5, 150 mM NaCl, 2% w/v BSA. Micropipettes for stimulatory beads and CTLs were prepared from borosilicate glass capillaries (1 mm OD, 0.78 mm ID, Harvard Apparatus). Imaging was carried out in an open top, environmentally controlled chamber mounted on an inverted microscope (Nikon TE300) equipped with a 100× objective lens. The rigid CTL micropipette was attached to a motorized micromanipulator (MP285, Sutter Instruments) and the bead micropipette to manual micrometers (Thorlabs). Beads were aspirated into the tip of the calibrated micropipette by applying ~6 kPa aspiration pressure using a syringe (typically 1 ml air volume depression). Two hundred pascals of pressure (applied using a water reservoir) was used to aspirate a CTL into the tip of the rigid pipette. Time-lapse recordings were started just before the CTL was gently brought into contact with the bead. In general, 50 ms brightfield exposures were taken at 2-s intervals for 3–5 min using Micromanager software. The deflection of the flexible micropipette was determined by tracking the position of the bead using a customized ImageJ macro (Husson et al., 2011). Bead position was determined with a precision of <60 nm, corresponding to a precision in force better than 6 pN for probe bending stiffness k = 0.1 nN/μm.

Micropillar Force Assay

PDMS (Sylgard 184, Dow Corning) micropillar arrays coated with H2-K^b-OVA and ICAM1 were prepared from silicon masters as described previously (Bashour et al., 2014). All pillars were 0.7 μm in diameter, 6 μm tall, and spaced hexagonally with a 2 μm center-to-center distance. Imaging experiments were conducted using an inverted fluorescence microscope (Olympus IX-81) fitted with a 100× objective lens (Olympus). Prior to imaging, CTLs were stained with

a fluorescently labeled (Alexa488 or Alexa647) anti-CD45 F_{ab} (clone 104-2, MSKCC Antibody and Bioresource Core) fragment to enable visualization of the cell membrane. They were then applied to the arrays and the cells and pillars imaged at the focal plane of the pillar tops. The CTL footprint on the pillar array (determined from the anti-CD45 F_{ab} signal) was used to identify pillars in contact with the CTL at each time point. Deflections were derived from the imaging data using custom MATLAB scripts as described previously (Bashour et al., 2014).

Cellular Perforation Assay

Twenty-four hours prior to imaging, B16-F10 cells were plated at 10^4 cells/100 μl/well in either fibronectin-coated 96-well plates (Costar) or in 96-well flat-bottom plates coated with polyacrylamide hydrogels (Matrigen) and fibronectin. One hour prior to imaging, cells were transferred into C^+ buffer (Hank's balanced salt solution [HBSS] with 10 mM HEPES pH 7.2, 4 mM $CaCl_2$, 2 mM $MgCl_2$, 0.4% BSA) containing Hoechst 33342 stain (1:2,000, Invitrogen). PI (100 μM final concentration) was added along with Blebbistatin (Sigma) or Latrunculin A (Sigma) as necessary. After 5 min, Hoechst and PI images were collected at 2-min intervals for 30 min using an inverted wide-field microscope (Zeiss Axiovert 200M, Metamorph acquisition software) fitted with a 5× objective lens (Zeiss). Dilutions of purified perforin in 50 μl C^- buffer (HBSS, 10 mM HEPES pH 7.2, 1 mM EGTA, 0.4% BSA) were added 4 min into the imaging run. To vary tonicity, hypertonic (+150 mM sucrose) or hypotonic (H_2O instead of HBSS) C^+ and C^- buffers were used instead of isotonic C^+ and C^-.

CTL-Target Cell Imaging in Microwells

PDMS grids containing 50 × 50 × 25 μm wells were submerged in imaging medium and seeded with CFSE-labeled RMA-s cells that had been pulsed with 1 μM OVA. In general, individual wells contained one to three RMA-s cells; 100 μM PI (Life Technologies) was added to the medium to enable real-time visualization of perforated cells. Then, CTLs expressing shNT or shPTEN together with CFP were added and the cells imaged using a 20× objective lens (Olympus) at 6-min intervals for 8 hr. Brightfield, GFP, CFP, and PI images were collected at each time point. Quantification was restricted to target cells forming synapses with only one T cell during the first 6 hr of the imaging experiment. All cells in this category were scored for the time of initial IS formation and also for the first appearance of PI signal above background.

SUPPLEMENTAL INFORMATION

Supplemental Information includes Supplemental Experimental Procedures, six figures, and five movies and can be found with this article online at http://dx.doi.org/10.1016/j.cell.2016.01.021.

AUTHOR CONTRIBUTIONS

R.B., B.M.W., J.H., A.L.F., W.J., A.O.-Y., N.B., L.C.K., and M.H. designed the experiments. R.B., B.M.W., J.H., A.L.F., W.J., A.O.-Y., and M.H. collected the data. R.B., B.M.W., J.H., A.L.F., A.O.-Y., and M.H. analyzed the data. F.D. and J.L. provided assistance with purified perforin. G.G. and C.H. contributed key insights. M.H., R.B., and L.C.K. wrote the manuscript.

ACKNOWLEDGMENTS

We thank N. Bantilan and M. Kaissar for technical support; U. Bandyopadhyay and M. Overholtzer for assistance with nitrogen cavitation; A. Gondarenko for assistance with micropillar fabrication; the Molecular Cytology Core Facility for help with imaging; the Antibody and Bioresource Core Facility for fluorescently conjugated F_{ab} fragments; S. Budhu and J. Wolchok for providing B16 cells; E. Mace and J. Orange for pHluorin-Lamp1; S. Rudensky and K. Pham for critical reading of the manuscript; and members of the M.H., L.C.K., M.O. Li, and G. Altan-Bonnet labs for advice. This work was supported in part by the NIH (R01-AI087644 to M.H., R01-AI088377 to L.C.K., PN2-EY016586 to L.C.K., and P30-CA008748 to Memorial Sloan-Kettering Cancer Center), the AXA-Ecole Polytechnique Chair (J.H.), Labex LaSIPS MECALEUCO (J.H.), the French National Research Agency (ANR-13-BSV2-0018 to C.H.), the French Foundation for Medical Research (FRM DEQ20140329513 to C.H.), the Geoffrey Beene Cancer Research Center (M.H.), the Starr Cancer Consortium (M.H.), and the Leukemia and Lymphoma Society (M.H.).

Received: September 23, 2015
Revised: December 9, 2015
Accepted: January 13, 2016
Published: February 25, 2016

REFERENCES

Babich, A., Li, S., O'Connor, R.S., Milone, M.C., Freedman, B.D., and Burkhardt, J.K. (2012). F-actin polymerization and retrograde flow drive sustained PLCγ1 signaling during T cell activation. J. Cell Biol. *197*, 775–787.

Bashour, K.T., Gondarenko, A., Chen, H., Shen, K., Liu, X., Huse, M., Hone, J.C., and Kam, L.C. (2014). CD28 and CD3 have complementary roles in T-cell traction forces. Proc. Natl. Acad. Sci. USA *111*, 2241–2246.

Beal, A.M., Anikeeva, N., Varma, R., Cameron, T.O., Vasiliver-Shamis, G., Norris, P.J., Dustin, M.L., and Sykulev, Y. (2009). Kinetics of early T cell receptor signaling regulate the pathway of lytic granule delivery to the secretory domain. Immunity *31*, 632–642.

Bertrand, F., Müller, S., Roh, K.H., Laurent, C., Dupré, L., and Valitutti, S. (2013). An initial and rapid step of lytic granule secretion precedes microtubule organizing center polarization at the cytotoxic T lymphocyte/target cell synapse. Proc. Natl. Acad. Sci. USA *110*, 6073–6078.

Brown, A.C., Oddos, S., Dobbie, I.M., Alakoskela, J.M., Parton, R.M., Eissmann, P., Neil, M.A., Dunsby, C., French, P.M., Davis, I., and Davis, D.M. (2011). Remodelling of cortical actin where lytic granules dock at natural killer cell immune synapses revealed by super-resolution microscopy. PLoS Biol. *9*, e1001152.

Bunnell, S.C., Kapoor, V., Trible, R.P., Zhang, W., and Samelson, L.E. (2001). Dynamic actin polymerization drives T cell receptor-induced spreading: a role for the signal transduction adaptor LAT. Immunity *14*, 315–329.

Chan, C.E., and Odde, D.J. (2008). Traction dynamics of filopodia on compliant substrates. Science *322*, 1687–1691.

Comrie, W.A., Babich, A., and Burkhardt, J.K. (2015). F-actin flow drives affinity maturation and spatial organization of LFA-1 at the immunological synapse. J. Cell Biol. *208*, 475–491.

Dai, J., and Sheetz, M.P. (1995). Mechanical properties of neuronal growth cone membranes studied by tether formation with laser optical tweezers. Biophys. J. *68*, 988–996.

Diz-Muñoz, A., Fletcher, D.A., and Weiner, O.D. (2013). Use the force: membrane tension as an organizer of cell shape and motility. Trends Cell Biol. *23*, 47–53.

Dustin, M.L., Chakraborty, A.K., and Shaw, A.S. (2010). Understanding the structure and function of the immunological synapse. Cold Spring Harb. Perspect. Biol. *2*, a002311.

Engler, A.J., Sen, S., Sweeney, H.L., and Discher, D.E. (2006). Matrix elasticity directs stem cell lineage specification. Cell *126*, 677–689.

Feinerman, O., Jentsch, G., Tkach, K.E., Coward, J.W., Hathorn, M.M., Sneddon, M.W., Emonet, T., Smith, K.A., and Altan-Bonnet, G. (2010). Single-cell quantification of IL-2 response by effector and regulatory T cells reveals critical plasticity in immune response. Mol. Syst. Biol. *6*, 437.

Grakoui, A., Bromley, S.K., Sumen, C., Davis, M.M., Shaw, A.S., Allen, P.M., and Dustin, M.L. (1999). The immunological synapse: a molecular machine controlling T cell activation. Science *285*, 221–227.

Grupp, S.A., and June, C.H. (2011). Adoptive cellular therapy. Curr. Top. Microbiol. Immunol. *344*, 149–172.

Guck, J., Schinkinger, S., Lincoln, B., Wottawah, F., Ebert, S., Romeyke, M., Lenz, D., Erickson, H.M., Ananthakrishnan, R., Mitchell, D., et al. (2005). Optical deformability as an inherent cell marker for testing malignant transformation and metastatic competence. Biophys. J. *88*, 3689–3698.

Hammer, J.A., 3rd, and Burkhardt, J.K. (2013). Controversy and consensus regarding myosin II function at the immunological synapse. Curr. Opin. Immunol. *25*, 300–306.

Hou, H.W., Li, Q.S., Lee, G.Y., Kumar, A.P., Ong, C.N., and Lim, C.T. (2009). Deformability study of breast cancer cells using microfluidics. Biomed. Microdevices *11*, 557–564.

Houk, A.R., Jilkine, A., Mejean, C.O., Boltyanskiy, R., Dufresne, E.R., Angenent, S.B., Altschuler, S.J., Wu, L.F., and Weiner, O.D. (2012). Membrane tension maintains cell polarity by confining signals to the leading edge during neutrophil migration. Cell *148*, 175–188.

Huang, H.W., Chen, F.Y., and Lee, M.T. (2004). Molecular mechanism of Peptide-induced pores in membranes. Phys. Rev. Lett. *92*, 198304.

Hui, K.L., Balagopalan, L., Samelson, L.E., and Upadhyaya, A. (2015). Cytoskeletal forces during signaling activation in Jurkat T-cells. Mol. Biol. Cell *26*, 685–695.

Huse, M., Lillemeier, B.F., Kuhns, M.S., Chen, D.S., and Davis, M.M. (2006). T cells use two directionally distinct pathways for cytokine secretion. Nat. Immunol. *7*, 247–255.

Husson, J., Chemin, K., Bohineust, A., Hivroz, C., and Henry, N. (2011). Force generation upon T cell receptor engagement. PLoS ONE *6*, e19680.

Ingber, D.E. (2006). Cellular mechanotransduction: putting all the pieces together again. FASEB J. *20*, 811–827.

Jacobelli, J., Chmura, S.A., Buxton, D.B., Davis, M.M., and Krummel, M.F. (2004). A single class II myosin modulates T cell motility and stopping, but not synapse formation. Nat. Immunol. *5*, 531–538.

Keefe, D., Shi, L., Feske, S., Massol, R., Navarro, F., Kirchhausen, T., and Lieberman, J. (2005). Perforin triggers a plasma membrane-repair response that facilitates CTL induction of apoptosis. Immunity *23*, 249–262.

Le Floc'h, A., and Huse, M. (2015). Molecular mechanisms and functional implications of polarized actin remodeling at the T cell immunological synapse. Cell. Mol. Life Sci. *72*, 537–556.

Le Floc'h, A., Tanaka, Y., Bantilan, N.S., Voisinne, G., Altan-Bonnet, G., Fukui, Y., and Huse, M. (2013). Annular PIP3 accumulation controls actin architecture and modulates cytotoxicity at the immunological synapse. J. Exp. Med. *210*, 2721–2737.

Lee, M.T., Hung, W.C., Chen, F.Y., and Huang, H.W. (2008). Mechanism and kinetics of pore formation in membranes by water-soluble amphipathic peptides. Proc. Natl. Acad. Sci. USA *105*, 5087–5092.

Lee, C.Y., Herant, M., and Heinrich, V. (2011). Target-specific mechanics of phagocytosis: protrusive neutrophil response to zymosan differs from the uptake of antibody-tagged pathogens. J. Cell Sci. *124*, 1106–1114.

Liu, X., Kapoor, T.M., Chen, J.K., and Huse, M. (2013). Diacylglycerol promotes centrosome polarization in T cells via reciprocal localization of dynein and myosin II. Proc. Natl. Acad. Sci. USA *110*, 11976–11981.

Liu, B., Chen, W., Evavold, B.D., and Zhu, C. (2014). Accumulation of dynamic catch bonds between TCR and agonist peptide-MHC triggers T cell signaling. Cell *157*, 357–368.

Lo, C.M., Wang, H.B., Dembo, M., and Wang, Y.L. (2000). Cell movement is guided by the rigidity of the substrate. Biophys. J. *79*, 144–152.

Lopez, J.A., Susanto, O., Jenkins, M.R., Lukoyanova, N., Sutton, V.R., Law, R.H., Johnston, A., Bird, C.H., Bird, P.I., Whisstock, J.C., et al. (2013). Perforin forms transient pores on the target cell plasma membrane to facilitate rapid access of granzymes during killer cell attack. Blood *121*, 2659–2668.

Masters, T.A., Pontes, B., Viasnoff, V., Li, Y., and Gauthier, N.C. (2013). Plasma membrane tension orchestrates membrane trafficking, cytoskeletal remodeling, and biochemical signaling during phagocytosis. Proc. Natl. Acad. Sci. USA *110*, 11875–11880.

Müller, A.J., Filipe-Santos, O., Eberl, G., Aebischer, T., Späth, G.F., and Bousso, P. (2012). CD4+ T cells rely on a cytokine gradient to control intracellular pathogens beyond sites of antigen presentation. Immunity *37*, 147–157.

Natkanski, E., Lee, W.Y., Mistry, B., Casal, A., Molloy, J.E., and Tolar, P. (2013). B cells use mechanical energy to discriminate antigen affinities. Science *340*, 1587–1590.

Oakes, P.W., Patel, D.C., Morin, N.A., Zitterbart, D.P., Fabry, B., Reichner, J.S., and Tang, J.X. (2009). Neutrophil morphology and migration are affected by substrate elasticity. Blood *114*, 1387–1395.

Orr, A.W., Helmke, B.P., Blackman, B.R., and Schwartz, M.A. (2006). Mechanisms of mechanotransduction. Dev. Cell *10*, 11–20.

Ostergaard, H.L., Kane, K.P., Mescher, M.F., and Clark, W.R. (1987). Cytotoxic T lymphocyte mediated lysis without release of serine esterase. Nature *330*, 71–72.

Paszek, M.J., Zahir, N., Johnson, K.R., Lakins, J.N., Rozenberg, G.I., Gefen, A., Reinhart-King, C.A., Margulies, S.S., Dembo, M., Boettiger, D., et al. (2005). Tensional homeostasis and the malignant phenotype. Cancer Cell *8*, 241–254.

Pipkin, M.E., and Lieberman, J. (2007). Delivering the kiss of death: progress on understanding how perforin works. Curr. Opin. Immunol. *19*, 301–308.

Polozov, I.V., Anantharamaiah, G.M., Segrest, J.P., and Epand, R.M. (2001). Osmotically induced membrane tension modulates membrane permeabilization by class L amphipathic helical peptides: nucleation model of defect formation. Biophys. J. *81*, 949–959.

Rabinovich, G.A., Gabrilovich, D., and Sotomayor, E.M. (2007). Immunosuppressive strategies that are mediated by tumor cells. Annu. Rev. Immunol. *25*, 267–296.

Rak, G.D., Mace, E.M., Banerjee, P.P., Svitkina, T., and Orange, J.S. (2011). Natural killer cell lytic granule secretion occurs through a pervasive actin network at the immune synapse. PLoS Biol. *9*, e1001151.

Ritter, A.T., Asano, Y., Stinchcombe, J.C., Dieckmann, N.M., Chen, B.C., Gawden-Bone, C., van Engelenburg, S., Legant, W., Gao, L., Davidson, M.W., et al. (2015). Actin depletion initiates events leading to granule secretion at the immunological synapse. Immunity *42*, 864–876.

Sage, P.T., Varghese, L.M., Martinelli, R., Sciuto, T.E., Kamei, M., Dvorak, A.M., Springer, T.A., Sharpe, A.H., and Carman, C.V. (2012). Antigen recognition is facilitated by invadosome-like protrusions formed by memory/effector T cells. J. Immunol. *188*, 3686–3699.

Sanderson, N.S., Puntel, M., Kroeger, K.M., Bondale, N.S., Swerdlow, M., Iranmanesh, N., Yagita, H., Ibrahim, A., Castro, M.G., and Lowenstein, P.R. (2012). Cytotoxic immunological synapses do not restrict the action of interferon-γ to antigenic target cells. Proc. Natl. Acad. Sci. USA *109*, 7835–7840.

Stinchcombe, J.C., and Griffiths, G.M. (2007). Secretory mechanisms in cell-mediated cytotoxicity. Annu. Rev. Cell Dev. Biol. *23*, 495–517.

Stinchcombe, J.C., Majorovits, E., Bossi, G., Fuller, S., and Griffiths, G.M. (2006). Centrosome polarization delivers secretory granules to the immunological synapse. Nature *443*, 462–465.

Thiery, J., Keefe, D., Boulant, S., Boucrot, E., Walch, M., Martinvalet, D., Goping, I.S., Bleackley, R.C., Kirchhausen, T., and Lieberman, J. (2011). Perforin pores in the endosomal membrane trigger the release of endocytosed granzyme B into the cytosol of target cells. Nat. Immunol. *12*, 770–777.

Ueda, H., Morphew, M.K., McIntosh, J.R., and Davis, M.M. (2011). CD4+ T-cell synapses involve multiple distinct stages. Proc. Natl. Acad. Sci. USA *108*, 17099–17104.

Wakatsuki, T., Schwab, B., Thompson, N.C., and Elson, E.L. (2001). Effects of cytochalasin D and latrunculin B on mechanical properties of cells. J. Cell Sci. *114*, 1025–1036.

Woodsworth, D.J., Dunsing, V., and Coombs, D. (2015). Design parameters for granzyme-mediated cytotoxic lymphocyte target-cell killing and specificity. Biophys. J. *109*, 477–488.

Xu, W., Mezencev, R., Kim, B., Wang, L., McDonald, J., and Sulchek, T. (2012). Cell stiffness is a biomarker of the metastatic potential of ovarian cancer cells. PLoS ONE *7*, e46609.

Yi, J., Wu, X.S., Crites, T., and Hammer, J.A., 3rd. (2012). Actin retrograde flow and actomyosin II arc contraction drive receptor cluster dynamics at the immunological synapse in Jurkat T cells. Mol. Biol. Cell *23*, 834–852.

Supplemental Figures

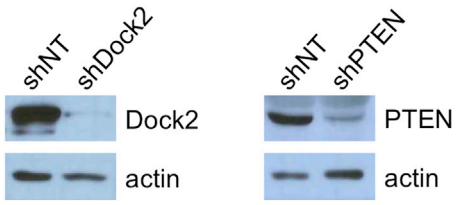

Figure S1. shRNA-Mediated Suppression of Dock2 and PTEN, Related to Figure 1

Representative western blots showing typical levels of Dock2 and PTEN depletion in OT1 CTLs expressing shDock2 and shPTEN, respectively, relative to controls expressing shNT. Actin served as a loading control. Data are representative of at least 5 independent experiments.

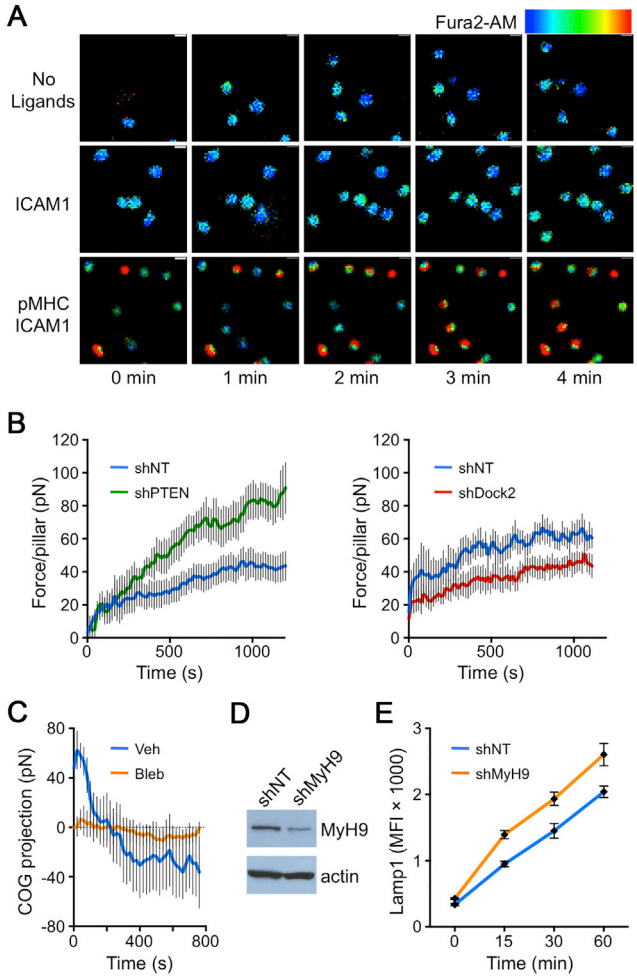

Figure S2. Antigen-Induced Forces on PDMS Micropillar Arrays, Related to Figure 3

(A) OT1 CTLs were loaded with Fura2-AM and then imaged on micropillars coated with the indicated ligands (pMHC = H2-K^b-OVA). Representative time-lapse montages are shown of CTLs coming into contact with the surface. Images are pseudocolored with warmer colors (e.g., orange, red) indicating higher concentrations of intracellular Ca^{2+}. Scale bars, 10 μm.

(B) CTLs expressing shNT, shDock2, and shPTEN were imaged on micropillar arrays coated with H2-K^b-OVA and ICAM1. Graphs show average force exertion per pillar versus time. n ≥ 6 cells per sample.

(C) CTLs treated with 50 μM blebbistatin (Bleb) or vehicle control (Veh) were imaged on stimulatory micropillar arrays. The average COG projection (see Figure 3C) for cells in each condition is plotted against time. Positive values indicate centrifugal "spreading," while negative values indicate centripetal "squeezing."

(D) Representative western blot showing typical levels of MyH9 relative to controls expressing shNT. Actin served as a loading control.

(E) OT1 CTLs expressing the indicated shRNAs were mixed with OVA-loaded RMA-s target cells and degranulation assessed at various times by surface exposure of Lamp1. Although shMyH9-expressing CTLs displayed increased degranulation in this experiment, the result was not consistent. All error bars denote SEM. Data are representative of at least two independent experiments.

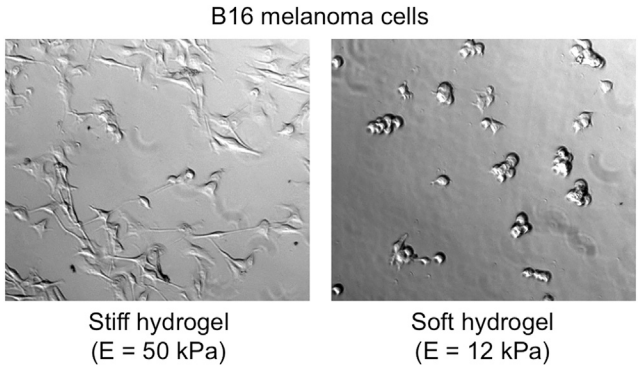

Figure S3. Hydrogel Stiffness Controls Cell Morphology, Related to Figure 5

B16 cells were cultured overnight on fibronectin-coated hydrogels of varying elasticity. Representative brightfield images show that cells spread on stiff (E = 50 kPa) substrates and adopt a more collapsed morphology on soft (E = 12 kPa) matrices. Data are representative of five independent experiments.

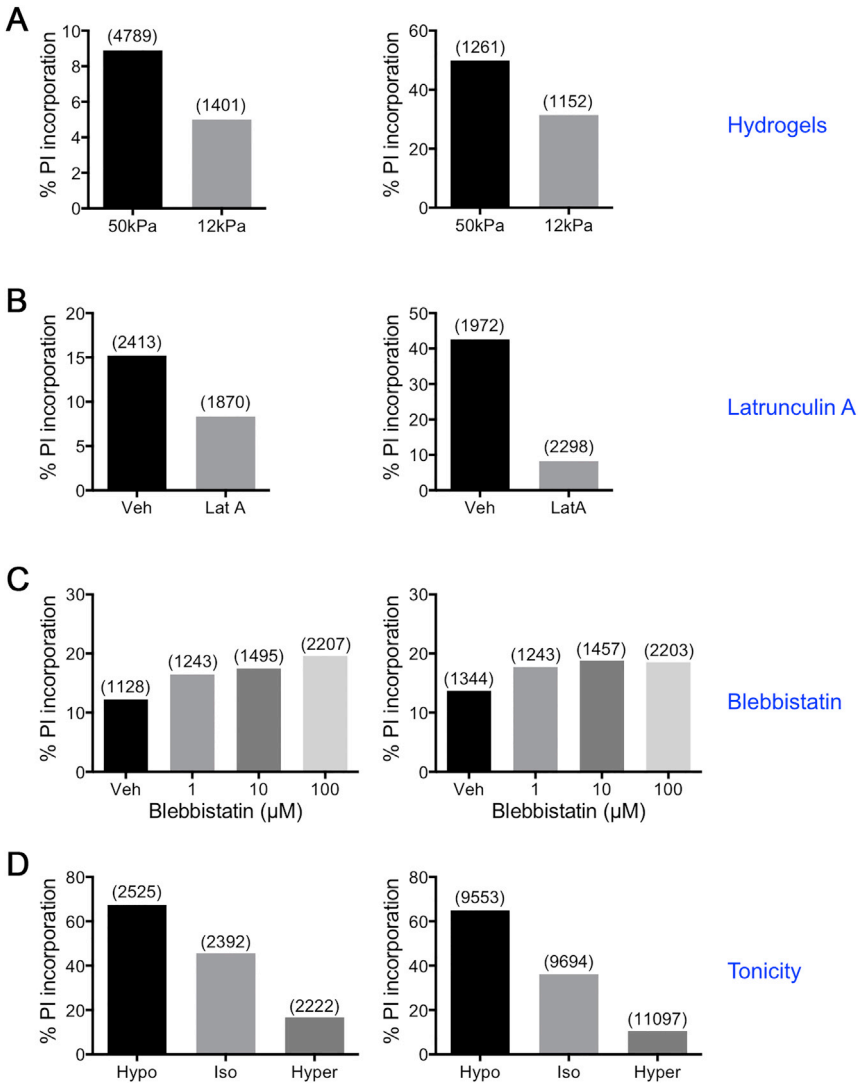

Figure S4. Cell Tension Modulates Perforin Pore Formation, Related to Figures 5 and 6

Replicate experiments for Figures 5C, 6B, and 6D.

(A) Quantification of perforin pore formation in B16 cells grown on stiff (E = 50 kPa) or soft (E = 12 kPa) fibronectin-coated hydrogels.

(B) Quantification of perforin pore formation in the presence of 7.5 μM latrunculin A (Lat A) or vehicle control (Veh).

(C) Quantification of perforin pore formation in the presence of the indicated concentrations of blebbistatin (Bleb) or Veh.

(D) Quantification of perforin pore formation in hypertonic (Hyper), hypotonic (Hypo), and isotonic (Iso) medium. A 1:1000 dilution of perforin was used in all experiments except the left graph in (A), which was performed using a 1:25 dilution of a low concentration prep. In all graphs, total cell counts are shown in parentheses above each bar.

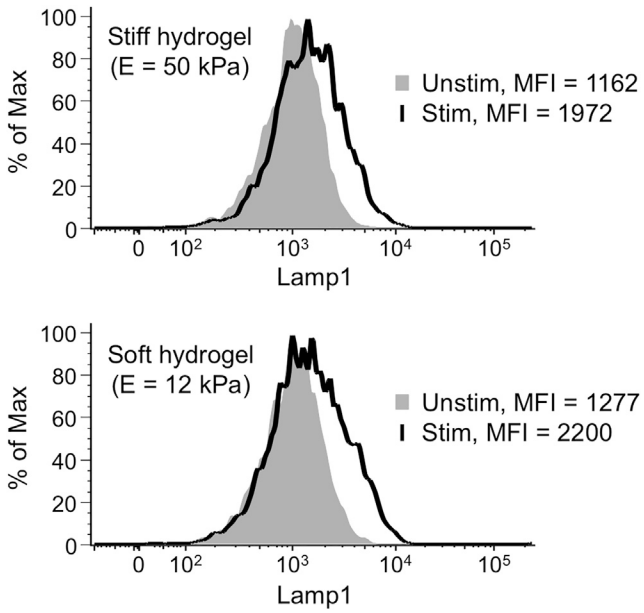

Figure S5. Matrix Stiffness Does Not Alter TCR-Induced Degranulation, Related to Figure 5

B16 cells were cultured overnight on fibronectin-coated hydrogels, loaded with OVA as necessary, and then mixed with OT1 CTLs. Representative histogram plots show T cell degranulation on stiff (50 kPa, above) or soft (12 kPa, below) matrices, as assessed by Lamp1 staining. Unstimulated samples (Unstim, no OVA) are shown in solid gray, and stimulated samples (Stim, OVA) in black outline. Mean Fluorescence Intensity (MFI) is indicated for each curve. Data are representative of two independent experiments.

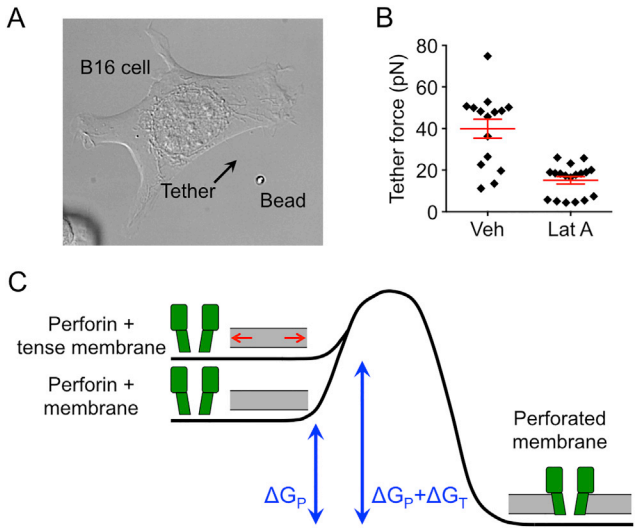

Figure S6. Membrane Tension of B16 Target Cells, Related to Figure 7

(A) DIC image showing a membrane tether connecting a B16 cell to a 2 μm diameter polystyrene bead, which is held in an optical trap.

(B) Membrane tethers were generated from B16 cells treated with 5 μM Latrunculin A (Lat A) or vehicle control (Veh) as indicated. Tether forces were determined from the displacement of the bead within the optical trap ($n \geq 15$ for each sample).

(C) Schematic diagram of the reaction coordinate for perforin pore formation in a membrane, illustrating how increased membrane tension can effectively reduce the activation barrier of the process. ΔG_P = free energy of pore formation, ΔG_T = free energy of tension release.

Cell, Volume *165*

Supplemental Information

Cytotoxic T Cells Use Mechanical Force to Potentiate Target Cell Killing

Roshni Basu, Benjamin M. Whitlock, Julien Husson, Audrey Le Floc'h, Weiyang Jin, Alon Oyler-Yaniv, Farokh Dotiwala, Gregory Giannone, Claire Hivroz, Nicolas Biais, Judy Lieberman, Lance C. Kam, and Morgan Huse

SUPPLEMENTAL EXPERIMENTAL PROCEDURES

Cells. The animal protocols used for this study were approved by the Institutional Animal Care and Use Committee of Memorial Sloan-Kettering Cancer Center. CTLs were prepared by mixing T cells from OT1 αβTCR transgenic mice (Taconic) with irradiated congenic splenocytes pulsed with 100 nM OVA and cultured in RPMI medium containing 10 % (vol/vol) FCS. Cells were supplemented with interleukin 2 (IL-2, 30 IU/ml) after 24 h and were split as needed in RPMI containing IL-2. B16-F10 cells were maintained in DMEM containing 10 % (vol/vol) FCS, while RMA-s and EL4 cells were grown in RPMI containing 10 % (vol/vol) FCS.

Retroviral transduction. Expression constructs for shNT, shDock2, shPTEN, shMyH9, and pHluorin-Lamp1 have been described (Le Floc'h et al., 2013; Liu et al., 2013; Rak et al., 2011). To prepare retrovirus, Phoenix E cells were transfected with expression vectors together with packaging plasmids using the calcium phosphate method. Ecotropic viral supernatants were collected after 48 h at 37°C and added to OT1 blasts 2 days after primary peptide stimulation. Mixtures were centrifuged at 1400 × g in the presence of polybrene (4 μg/ml) at 35 °C. T cells were then split 1:3 in medium containing IL-2.

CTL-target cell imaging in microwells. PDMS grids containing 50×50×25 μm wells were submerged in imaging medium and seeded with CFSE-labeled RMA-s cells that had been pulsed with 1 μM OVA. In general, individual wells contained 1-3 RMA-s cells. 100 μM PI (Life Technologies) was added to the medium to enable real time visualization of perforated cells. At low PI concentrations (e.g. 2 μM), strong fluorescence is only observed after a sustained loss of membrane integrity. At high concentrations (~100 μM), however, PI can be used to detect the initiation of perforin pores (Lopez et al., 2013). CTLs expressing shNT or shPTEN together with CFP were added and the cells imaged using a 20× objective lens (Olympus) at 6 min intervals for 8 hr. Brightfield, GFP, CFP, and PI images were collected at each time point. Quantification was restricted to target cells forming synapses with only one T cell during the first 6 hours of the imaging experiment. All cells in this category were scored for the time of initial IS formation and also for the first appearance of PI signal above background.

Micropipette preparation and calibration. Tapered micropipettes were prepared by pulling borosilicate glass capillaries (1 mm OD, 0.78 mm ID, Harvard Apparatus) with a P-97 device (Sutter Instruments). A microforge (MF-200, WPI) was used to cut the bead micropipette and the rigid CTL micropipette at the desired diameters (typically 1 μm and 3 μm, respectively). Another microforge (MF-900, Narishige) was then used to introduce a 90° bend at the end of the bead micropipette. 45° angles were also introduced into the bodies of both pipettes to position their extremities orthogonal to the imaging plane during experiments. The bending stiffness k of the bead micropipette was measured by pushing its tip against the tip of a thicker micropipette of known stiffness. A single-axis piezo translation stage (Thorlabs) was used to move the bead micropipette in a sinusoidal fashion and the position of each tip was detected at 30Hz using a home-made Labview program (National Instruments). The observed ratio of pipette deflections was then used to deduce the stiffness of the bead micropipette (typically k = 0.1 nN/μm).

Micropillar coating and data acquisition. For coating, arrays were washed with ethanol and phosphate buffered saline (PBS) and then incubated in Alexa568-labeled streptavidin (20 μg/ml in PBS) at room temperature for at least two hours. After further washing in PBS, the arrays were incubated with biotinylated H2-K^b-OVA and ICAM1 (each 20 μg/ml in PBS) for 2 hours at room temperature. The pillars were then washed into colorless RPMI containing 5% FCS (Imaging medium). Data acquisition was implemented using Metamorph software. For standard force quantification experiments (Figure 3), brightfield, Alexa488 (CTL), and Alexa568 (pillars) images were collected every 15 s. For degranulation experiments (Figure 7), brightfield, Alexa488 (degranulation), Alexa647 (CTL), and Alexa568 (pillars) images were collected every 20 s. Images were exported as tif files and aligned using a custom Matlab script.

Micropillar deflection analysis. Center of gravity (COG) projections of pillar deflections were determined by calculating the projection of each deflection along a line connecting the pillar to the COG of the CTL footprint. Degranulation events were identified as an abrupt increase in GFP fluorescence. To determine the DDP (Distance to Displaced Pillar) parameter for a degranulation event, average deflections were

determined for the time period beginning 40 s before degranulation and extending 120 s after. "Strongly deflected" pillars were then identified as pillars with mean deflections ≥ 0.75 × the mean deflection of the most strongly deflected pillar during this time frame. The distance between the degranulation position and the closest "strongly deflected" pillar was defined as the DDP. DDP values for degranulation events were compared to null distributions generated by performing the DDP calculation for every position in the CTL-array interface at the time of degranulation. Paired analysis of degranulation DDPs and mean DDPs from null distributions was carried out using Prism (GraphPad). Radial shell analysis was performed by determining the position of relevant pillars and degranulation events along a segment beginning at the COG of the interface (assigned a value of 0) and ending at the edge of the interface (assigned a value of 10). The mechanical energy required for pillar deflections was calculated using the following expression (E = Fd/2), where E is the energy, F is the force, and d is the length of the deflection.

Perforin purification and fibronectin coating for perforation assay. Human perforin was purified from YT-Indy cells as described (Thiery et al., 2010), but using the following modified relaxation buffer: 100 mM KCl, 3.5 mM $MgCl_2$, 10 mM PIPES pH 6.8, 1.25 mM EGTA, and 1 mM ATP. Perforin is a metastable, hydrophobic molecule with a tendency to aggregate. The overall activity of each preparation varied considerably, and the activity of any one preparation changed over the course of a few hours. To circumvent this issue, we collected each experimental condition either right before or right after its associated control, and switched the order of data collection in repeat experiments. This enabled us to observe robust relative changes, despite the day-to-day variation in overall perforin activity. For coating, plastic wells were incubated with 10 μg/ml fibronectin (Calbiochem) for 1 hr at 37°C, and polyacrylamide hydrogels (Matrigen) were incubated with 10 μg/ml fibronectin for 30 min at room temperature.

Lytic granule polarization. OT1 CTLs expressing shNT, shDock2, or shPTEN together with GFP were mixed 1:1 with EL4 thymoma cells that had been loaded with 1 μM OVA. After 10 min, cells were transferred into warm HBSS, attached to poly-D-lysine-coated coverslips, and fixed with 4% paraformaldehyde. After washing with PBS and permeabilization with 0.2% Triton X-100 in PBS, cells were blocked with PBS + 10% normal goat serum and then incubated in blocking buffer containing antibodies against Lamp1 (eBioscience, clone 1D4B, 1:200 dilution) and pericentrin (abcam, rabbit polyclonal, 1:200 dilution) overnight at 4°C. Cells were then washed in PBS and incubated in blocking buffer containing Alexa594 labeled anti-Rat antibodies and Alexa647 labeled anti-Rabbit antibodies (both 1:1000 dilution) for 2 hr at 4° C. After a final wash in PBS, Cells were mounted on glass slides and sealed. CTL-target cell conjugates were imaged using an inverted fluorescence microscope (Olympus IX-81) fitted with a 65× objective lens (Olympus). In addition to a brightfield image, z-stacks (1 μm increments, 20 μm total) of Alexa594, Alexa647, and GFP were collected for each field of view. Lytic granule polarization was quantified using projection images derived from the z-stack data. For each CTL, intensity thresholding was used to establish a mask encompassing the lytic granule compartment. Polarization of this mask toward the IS was then quantified by calculating a polarization index = (Distance between the IS and the center of gravity of the granule mask)/(Distance between the IS and the opposite side of the CTL). T-test analysis of the resulting distributions was performed in Prism.

RMA-s killing assay. RMA-s cells labeled with the membrane dye PKH26 (Sigma-Aldrich) were pulsed with varying concentrations of OVA and mixed 1:1 in 96-well plates with OT1 CTLs. After 6 hr at 37°C, samples were treated with 2.5 mM EDTA to disrupt conjugate formation and specific lysis of PKH26+ target cells was assessed by flow cytometry as described (Quann et al., 2009).

B16 cytotoxicity assay. B16-F10 cells were cultured overnight on fibronectin-coated hydrogels in the presence of 20 ng/ml IFNγ, which was included to induce upregulation of class I MHC. They were then loaded with 100 nM OVA for 1 hour and washed three times in lactate dehydrogenase (LDH) release assay medium (RPMI with 5% vol/vol FCS). OT1 CTLs were added at various effector to target (E:T) ratios and incubated for 5 hr at 37°C in LDH medium. Target cell death was quantified with an LDH cytotoxicity assay kit (Clontech) using the manufacturer's recommended protocol. All measurements were performed in triplicate. To assess degranulation responses, CTLs were added to B16-F10 cells at a 1:1 E:T ratio and incubated for 2 hr at 37°C in the presence of eFluor660 conjugated anti-Lamp1 antibody (1 μg/ml, Clone 1D4B, eBiosciences). Staining was quantified by flow cytometry. In staurosporine-induced apoptosis assays, B16 cells cultured on fibronectin-coated hydrogels were treated with varying concentrations of

staurosporine, and lysis was quantified by LDH release after 17 h at 37°C.

Immunoblot. 0.2-1 × 10^6 CTLs were lysed in ice cold buffer containing 10 mM TrisHCl, 5 mM EDTA, 1% NP-40, 0.5% sodium deoxycholate, and 0.15 M NaCl. Perforin expression was assessed using a rabbit polyclonal antibody (Cell Signaling). shRNA mediated suppression of Dock2, PTEN, and MyH9 were routinely confirmed using an anti-Dock2 polyclonal Ab (Millipore), an anti-PTEN monoclonal antibody (clone D4.3; Cell Signaling Technology), and an anti-MyH9 polyclonal antibody (BT-567; Biomedical Technologies). Actin served as a loading control (clone AC-15, Sigma).

Ca^{2+} imaging. CTLs were loaded with 5 μg/ml Fura-2AM and then added to glass or PDMS surfaces that had been coated with H2-K^b-OVA and ICAM1. Stimulatory PDMS was prepared as described above and glass surfaces were coated using an established protocol (Quann et al., 2009). Fura2 images using 340 nm and 380 nm excitation were acquired every 30 seconds for 20–30 min with a 20× objective lens (Olympus). Single cell Ca^{2+} responses were quantified by normalizing the Fura2 ratio of each cell using the last image before the initial rise in Ca^{2+}.

Quantification of membrane tension. Membrane tethers were generated from adherent B16 cells using 2 μm diameter concanavalin A-coated beads, which were prepared by mixing streptavidin microspheres with 40 μg concanavalin A per mg of beads. Using an optical trap (10 W 1064 nm laser (IPG), used at 0.8 W), individual beads were brought into contact with the cell membrane for ~ 2 s and then pulled away, generating a thin membrane tether connecting the bead to the cell surface. Each experiment was monitored continuously by differential interference contrast (DIC) imaging at 60× magnification in order to track the position of the bead and confirm tether formation. For each trial, tether force F was calculated using the trap stiffness k and the bead displacement within the trap, d, using the following equation (F=kd). Bead displacements within the trap were extracted from the imaging data using a custom ImageJ plugin, and trap stiffness was determined using an established calibration protocol (Simmons et al., 1996). Membrane tension values were derived from the force measurements using the following expression ($T = F^2/8B\pi^2$), where T is the membrane tension, F is the observed force, and B is the bending stiffness of the membrane (assumed to be 2 × 10^{-19} N-m)(Bo and Waugh, 1989; Heinrich and Waugh, 1996). The free energy difference ΔG for the formation of a peptide pore of radius r within a membrane under tension T relative to the formation of that same pore on an untensed membrane is given by $\Delta G = \pi r^2 T$.

SUPPLEMENTAL REFERENCES

Bo, L., and Waugh, R.E. (1989). Determination of bilayer membrane bending stiffness by tether formation from giant, thin-walled vesicles. Biophysical journal *55*, 509-517.
Heinrich, V., and Waugh, R.E. (1996). A piconewton force transducer and its application to measurement of the bending stiffness of phospholipid membranes. Annals of biomedical engineering *24*, 595-605.
Quann, E.J., Merino, E., Furuta, T., and Huse, M. (2009). Localized diacylglycerol drives the polarization of the microtubule-organizing center in T cells. Nat Immunol *10*, 627-635.
Simmons, R.M., Finer, J.T., Chu, S., and Spudich, J.A. (1996). Quantitative measurements of force and displacement using an optical trap. Biophysical journal *70*, 1813-1822.
Thiery, J., Walch, M., Jensen, D.K., Martinvalet, D., and Lieberman, J. (2010). Isolation of cytotoxic T cell and NK granules and purification of their effector proteins. Current protocols in cell biology / editorial board, Juan S Bonifacino [et al] *Chapter 3*, Unit3 37.